WATER RESOURCES RESEARCH, VOL. 34, NO. 12, PAGES 3235–3244, 1998

Mapping basin scale variable source areas from multitemporal remotely sensed observations of soil moisture behavior

Niko E. C. Verhoest and Peter A. Troch
Laboratory of Hydrology and Water Management, University of Gent, Gent, Belgium

Claudio Paniconi
Centro di Ricerca, Sviluppo e Studi Superiori in Sardegna, Cagliari, Italy

François P. De Troch
Laboratory of Hydrology and Water Management, University of Gent, Gent, Belgium

Abstract. Soil moisture is an important and highly variable component of the hydrologic cycle. Active microwave remote sensing offers the potential for frequent observation of soil moisture at basin and regional scales. Notwithstanding recent advances, the goal of obtaining accurate and reliable measurements or maps of soil moisture from these instruments remains elusive. The main difficulties for active sensors such as synthetic aperture radar (SAR) are the combined effects of soil moisture, surface roughness, and vegetation on the backscattered signal. We show that it is possible to separate soil moisture information from the other physical factors that dominate the radar backscattering, such as topography and land cover, through a principal component analysis of a time series of eight European Remote Sensing (ERS) SAR images. The soil moisture patterns observed in one of the principal components are consistent with the rainfall-runoff dynamics of a catchment and reflect the variable source areas occuring in the vicinity of the river network.

1. Introduction

The characterization of the spatial and temporal variability of soil moisture over large regions continues to receive much attention, reflecting both the significant influence this variability exerts on evapotranspiration and on rainfall-infiltration-runoff partitioning and the difficulties inherent in monitoring, measuring, and modeling the water content of near-surface soils [*Georgakakos and Baumer*, 1996].

At hillslope and catchment scales, soil moisture and its variability are fingerprints of several hydrologic processes. During rainy periods, flow convergence results in relatively low temporal variability of surface soil moisture in the vicinity of the drainage network. In contrast, areas located at or near hillslope tops will exhibit more pronounced soil moisture variation in time due to successive wetting during rainfall events and drying through evapotranspiration and redistribution during interstorm periods (Figure 1). Land surface–atmosphere exchange processes are also determined by available moisture content, with atmosphere-controlled evaporation typically occurring in or near discharge zones, while soil-controlled evaporation occurs more frequently in recharge zones [*Salvucci and Entekhabi*, 1995].

Remote sensing offers the potential for frequent observation of soil moisture at basin and regional scales. A variety of infrared and microwave (both active and passive) sensors operating from laboratory, aircraft, and satellite platforms have been tested for soil moisture retrieval, and the potentials and limitations of each of these remote sensing techniques are well-documented [*Choudhury*, 1991; *Blyth*, 1993; *Engman*, 1995].

Whereas recent studies have successfully demonstrated the use of infrared, passive microwave, and non-synthetic aperture radar (SAR) sensors to obtain soil moisture information [*Capehart and Carlson*, 1997; *Jackson*, 1997; *Wagner et al.*, 1996], the potential of active microwave remote sensing based on synthetic aperture radar instruments remains largely unrealized. The main advantage of radar is that it provides observations at a high spatial resolution of tens of meters compared to tens of kilometers for passive satellite instruments such as radiometers or non-SAR active instruments such as scatterometers. The main difficulty with SAR imagery is that soil moisture, surface roughness, and vegetation cover all have an important and nearly equal effect on radar backscatter. These interactions make retrieval of soil moisture possible only under particular conditions such as bare soil or surfaces with low-vegetation density [*Ulaby et al.*, 1982; *Cognard et al.*, 1995; *Altese et al.*, 1996].

It should be possible to separate the vegetation, topography, and soil moisture effects on radar response using multifrequency and/or multipolarization measurements [*Ulaby et al.*, 1996], but currently operational satellites are not equipped with sensors that provide such data. A related concept that can be applied to existing satellite imagery is multitemporal analysis. Multitemporal analysis based on statistical techniques such as filtering, differencing, and ratioing is commonly used in optical remote sensing for land use, forestry, and other applications [*Howarth and Wickware*, 1981; *Jenson and Toll*, 1982; *Singh*, 1989]. Although on its own it will not produce direct or absolute measurements, multitemporal analysis could be use-

Paper number 98WR02046.
0043-1397/98/98WR-02046$09.00

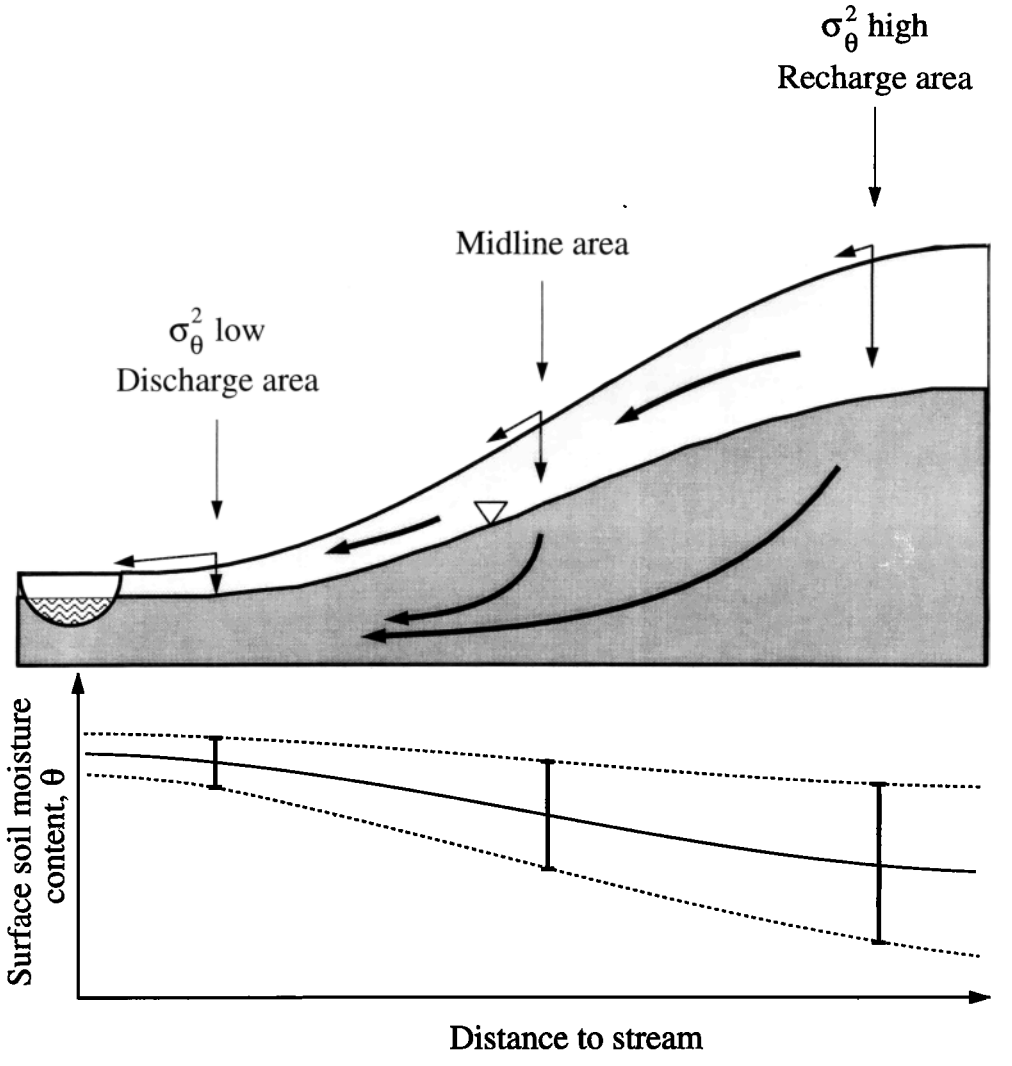

Figure 1. Moisture redistribution along a hillslope resulting in recharge areas with high temporal soil moisture variability and discharge areas with low temporal soil moisture variability (σ_θ^2 is the temporal variance of soil moisture).

ful for deriving wetness indices and for monitoring temporal changes or elucidating spatial patterns in soil moisture. In addition, such detection techniques may provide estimates or maps of other hydrologic features or parameters that are sensitive to or affect the spatial distribution of soil moisture, such as the extent of floodplains and recharge/discharge areas, soil texture and hydraulic characteristics [*Hollenbeck et al.*, 1996; *Mattikalli et al.*, 1996], and the time to onset of soil-limited (stage-two) evaporation [*Salvucci*, 1997; *Salvucci and Amano*, 1997].

In cases where vegetation and topographic effects are less prominent than soil moisture effects, simple statistical techniques, such as calculating the standard deviation for each pixel over a period of time, are able to reveal soil moisture patterns [*Rignot and van Zyl*, 1993; *Gineste et al.*, 1998]. Since such cases are atypical and cannot normally be identified a priori, a more robust technique is sought.

In this paper we use a multitemporal analysis based on the principal components transformation to show that the soil moisture information in SAR images can be separated from other physical factors that influence the radar response. The principal component analysis (PCA) is applied to a wintertime sequence of eight ERS (European Remote Sensing) satellite images acquired over the Zwalm catchment in Belgium. In the images constructed from the first three principal components, effects due to local incidence angle (topography), land cover (forests and urban areas), and soil moisture are isolated. The latter image displays spatial patterns that are consistent with soil moisture behavior expected from the runoff and drainage response of the basin to rainfall events. The potential applications of the methodology to mapping a catchment's partial contributing areas and discharge zones are discussed.

2. Description of Test Site and Available Data

The Zwalm catchment is situated about 20 km south of Gent in Belgium (50°45′48″N to 50°54′16″N and 3°40′17″E to 3°50′15″E). It is a fifth Strahler-order basin with a total drainage area of 114 km^2 and a drainage density of 1.55 km/km^2. Rolling hills and mild slopes, with a maximum elevation difference of 150 m, characterize the topography. Land use is mainly arable crop farming and permanent pasture, while the

south of the catchment is partly forested. The degree of urbanization is ~10% and is mainly clustered in three small towns. The soil type in the catchment is predominantly sandy loam, according to the Belgian Soil Map, with minor isolated patches of sand and clay. The climatic regime is humid temperate with a mean annual rainfall of 775 mm distributed almost uniformly over the year and a mean annual pan evapotranspiration of 450 mm. The catchment is described in detail by *De Troch* [1977].

The Zwalm catchment has been the subject of several remote sensing campaigns involving SAR instruments from airborne and spaceborne platforms [*De Troch et al.*, 1996, 1997; *Su et al.*, 1997]. For this study a sequence of eight ERS satellite precision images (PRI) was acquired over the Zwalm catchment during the winter period of 1995–1996 (see Table 1). Figure 2 shows a raw ERS 1 image of the Zwalm catchment taken on October 31, 1995. The ERS satellites carry several advanced instruments, such as the Active Microwave Instrument (AMI), which combines the functions of a synthetic aperture radar and a wind scatterometer. The SAR is a C band (5.3 GHz) radar operating in VV polarization [*Attema*, 1991] and has a spatial resolution of 30 × 30 m and a pixel size of 12.5 × 12.5 m. During the so-called "Tandem Phase," the ERS 1 and ERS 2 satellites were placed in the same sun-synchronous orbit at a nominal altitude of 785 km, such that the time difference between overpasses of ERS 1 and ERS 2 was exactly 24 hours. Wintertime images were selected for this study in order to minimize soil roughness and vegetation changes. Figure 3 shows the daily rainfall for the winter period together with the average backscattering coefficient over the whole catchment, calculated from tandem pairs of the eight ERS 1/2 images. From this figure it is already apparent that the scene information is strongly affected by the rainfall episodes.

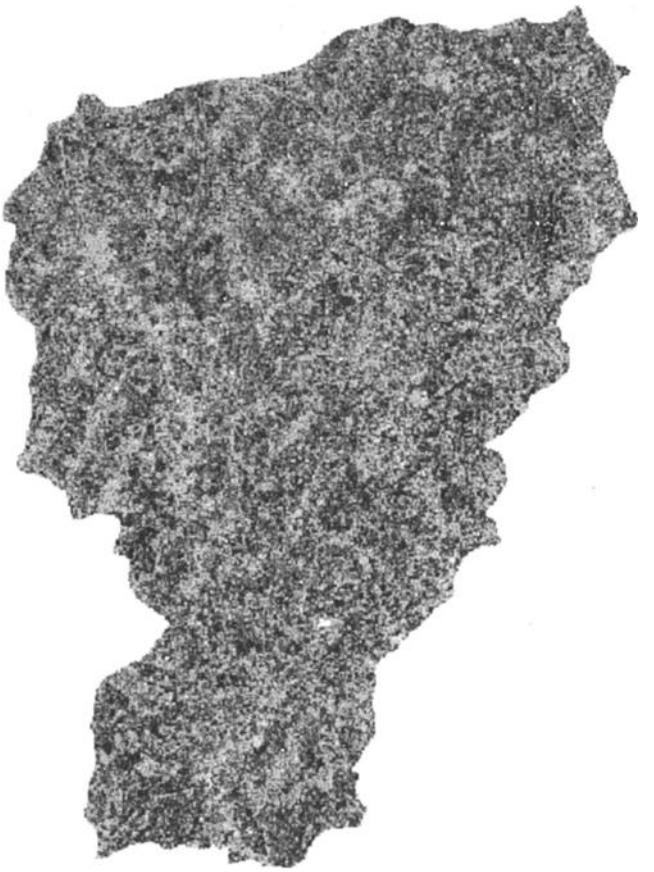

Figure 2. Raw ERS 1 image taken over the Zwalm catchment on October 31, 1995 [*European Space Agency*, 1992].

3. Processing of the SAR Images

3.1. Georeferencing

The eight images were transformed into the Lambert 7∠ coordinate system based on a previously georeferenced SPOT image. Ground control points (GCPs) were selected on the SPOT image, and their counterparts were identified on the ERS images. Over 15 points covering the whole scene were used for this purpose. On the basis of these GCPs a first-order affine transformation of the nongeoreferenced image into the new coordinate system was performed. At the same time, the images were resampled to 30 × 30 m (which is the actual scene spatial resolution), and only the area corresponding to the Zwalm watershed was retained. Standard georeferencing procedures for remotely sensed data are described by *Lillesand and Kiefer* [1994]. After georeferencing all eight images, the relative positional error between images was investigated. It was found that this error is of the order of less than one pixel (30 m).

Table 1. Identification of the Satellite Images Used in the Analysis

Date	Satellite	PAF
Oct. 31, 1995	ERS 1	D
Nov. 1, 1995	ERS 2	D
Dec. 5, 1995	ERS 1	I
Dec. 6, 1995	ERS 2	I
Feb. 13, 1996	ERS 1	I
Feb. 14, 1996	ERS 2	D
March 19, 1996	ERS 1	I
March 20, 1996	ERS 2	I

All Images Have Frame 2583 and Track 423. PAF stands for Processing and Archiving Facility, and here it is either German (D) or Italian (I).

3.2. Calibration

The ERS system can produce several products, one of these being SAR PRIs. This product is intended for multitemporal imaging and for deriving radar cross sections [*European Space Agency* (*ESA*), 1992]. SAR PRIs are subjected to engineering corrections and relative calibration to compensate for well-understood sources of system variability. Absolute calibration of the precision images has to be performed by the user. The following description of the calibration procedure used in this study is based on *Laur et al.* [1997]. The digital numbers in the PRIs are related to the backscattering coefficient through the following formulas:

$$A_{ij}^2 = \mathrm{DN}_{ij}^2 \frac{1}{K} \frac{\sin \alpha}{\sin \alpha_{ref}} C \frac{\mathrm{PRP}}{\mathrm{RRP}} \mathrm{PL} \tag{1}$$

and

$$\sigma^0 = \frac{1}{N} \sum_{i,j}^{N} A_{ij}^2 \tag{2}$$

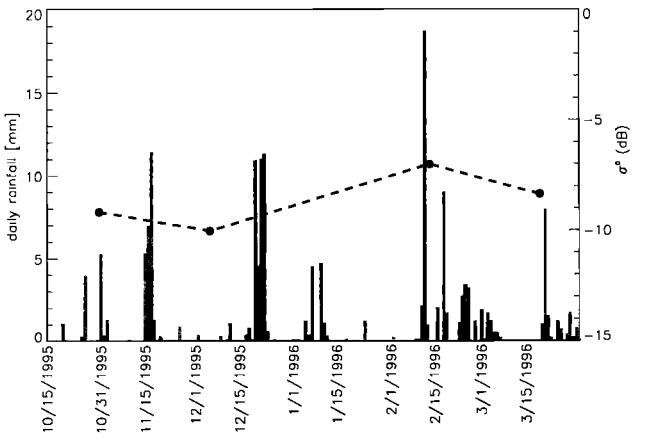

Figure 3. Daily rainfall for the 1995–1996 winter period. Also indicated by the dashed line and right-hand scale is the average radar backscatter σ^0 for the catchment calculated for each tandem pair of ERS 1/2 images.

for all pixels within the area of interest (AOI), where N is the number of pixels within the AOI, i.e., a group of pixels corresponding to a distributed target in the image (e.g., a bare soil field); i, j are the range and azimuth locations of the pixels within the distributed target containing N pixels; DN_{ij} is the digital number corresponding to the pixel at location (i, j); A_{ij} is the amplitude corresponding to the pixel at location (i, j); σ^0 is the backscattering coefficient corresponding to all N pixels within the AOI; K is a calibration constant; α is the average incidence angle corresponding to the AOI, which is calculated from the image geometry, the earth surface being represented by a reference ellipsoid (Goddard Earth Model, GEM 6); α_{ref} is the ERS reference incidence angle, i.e., 23.0°; C is a factor that accounts for updating the gain due to the elevation antenna pattern implemented in the processing of ERS SAR PRI data products ($C = 1$ for all ERS 1 PRI images processed after July 16, 1995, and for ERS 2 PRI products processed after October 16, 1995); PRP is the power of the replica pulse used to generate the PRI product and is given in the header file of the PRI image; RRP is the replica pulse power of a reference image taken over Flevoland (Netherlands); and PL is the analogue to digital convertor (ADC) power loss.

In (1), the term $(1/K)$ $(\sin \alpha/\sin \alpha_{ref})$ relates the digital number to the backscattering coefficient. The calibration constant, K, depends on the Processing and Archiving Facility (PAF) and is different for the two satellites. The other term (C)(PRP/RRP)(PL) represents the radiometric calibration of the signal. The C factor equals one for all eight images used in our analysis. The power replica pulse (PRP) correction, which has to be taken into account only for ERS 1 products, is determined by monitoring the power of copies of transmitted pulses (replica pulses), as they are passed through the SAR system and by comparing the replica pulse power (RRP) used to generate the image in question with that used to generate the reference image of Flevoland. Eventually, the images need to be also corrected for ADC saturation.

Since our test site is located near the mid-swath line of the PRI, many of the parameters can be set to their reference values [*Laur et al.*, 1997, pp. 27–40]. The parameter α was set to 23°. The slant range or distance from a particular pixel to the satellite, R_u, used for the calculation of the power loss, PL, was assumed to be the reference slant range, R_{ref} = 847.0 km. The suggested size of 5 × 15 km for the moving smoothing windows used to calculate PRP was replaced by an area covering the whole catchment due to the particular shape of the test site. More details on the calibration of the ERS images for the Zwalm catchment are given by *Verhoest* [1997].

For the PCA software used in this study (GRASS 4.1 [*Construction Engineering Research Laboratories (CERL)*, 1993]) it is necessary to work with integer images, therefore the local A_{ij} values were transformed back into a standardized DN using

$$DN_{ij}^{ref} = A_{ij}\sqrt{K_{ref}}$$

where K_{ref} is the calibration constant for the ERS 1 I-PAF, selected as our reference calibration constant. This insures that the eight images can be reliably and accurately compared to one another.

3.3. Speckle Filtering

Radar images of homogeneous rough surfaces always show a granular pattern called speckle. This noise-like phenomenon is the result of changes in the distances between elementary scatterers and the receiver caused by surface roughness [*Goodman*, 1976], so that the received waves, although coherent in frequency, are no longer coherent in phase. SAR systems rely upon the coherence properties of the scattered signals, making these systems susceptible to speckle to a much greater extent than is the case for noncoherent systems such as side-looking airborne radars [*Porcello et al.*, 1976]. The presence of speckle noise in an imaging system reduces the detectability of a target and also degrades the quality and interpretability of the image.

In SAR practice, speckle is suppressed by creating n look images. This reduces the standard deviation of speckle by a factor $\sqrt{n}$ but deteriorates the spatial resolution by a factor n [*Goodman*, 1976; *Ulaby et al.*, 1988; *Lee et al.*, 1994]. During the last decade, techniques that do not deteriorate resolution have been proposed for speckle reduction on processed radar images. This filtering requires the reduction of the variance within homogeneous areas, preservation of edges and lines, exclusion of point scatterers, preservation of spatial variability, and the avoidance of artefacts [*Schwan et al.*, 1995]. However, experiments indicate that there is always a trade-off between the smoothing of speckle and the preservation of useful information [*Shi and Fung*, 1994].

Lopes et al. [1990] developed an efficient speckle filter based on the assumption that the underlying scene intensity follows a gamma distribution (the gamma maximum a posteriori (MAP) filter). This filter leads to very high speckle reduction that allows a good radiometric classification [*Nezry et al.*, 1991]. Gamma MAP filtering using a 3 × 3 kernel was applied to the eight standardized DN images of the Zwalm catchment. The kernel size was chosen as small as possible in order not to smooth out relevant information, which occurs at pixel scale.

4. Multitemporal Analysis of the SAR Images

4.1. Principal Component Analysis

The principal components transformation is a standard tool in image enhancement, image compression, and classification [*Richards*, 1986; *Singh*, 1989; *Lee and Hoppel*, 1992]. It linearly transforms multispectral or multidimensional data into a new coordinate system in which the data can be represented without correlation. The new coordinate axes are orthogonal to

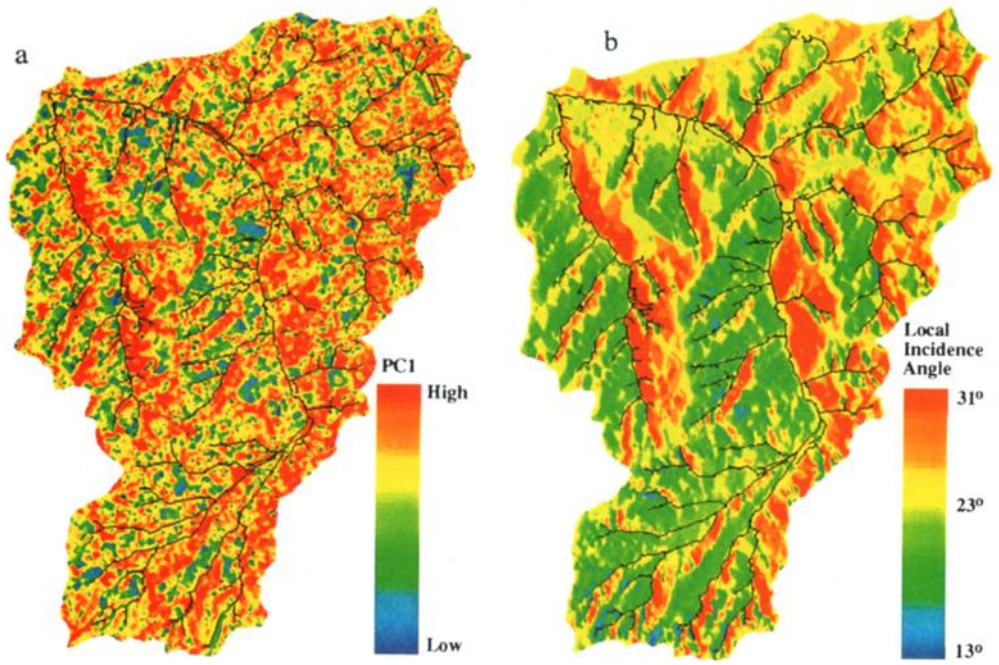

Plate 1. (a) First principal component image and (b) an image of the local incidence angles calculated from the digital elevation model of the catchment. The stream network (black) is shown in overlay in both images.

each other and point in the direction of decreasing order of the variances, so that the first principal component contains the largest percentage of the total variance (hence the maximum or dominant information), the second component contains the second largest percentage, and so on. Images transformed by PCA may make evident features that are not discernable in the original data, local details in multispectral images, changes, and trends in multitemporal data, which typically show up in the intermediate principal components.

PCA is widely used in optical remote sensing but less so in the more recent area of SAR image processing. One example is provided by *Lee and Hoppel* [1992], who used a modified principal component transformation on multifrequency polarimetric SAR imagery for reducing speckle and for informa-

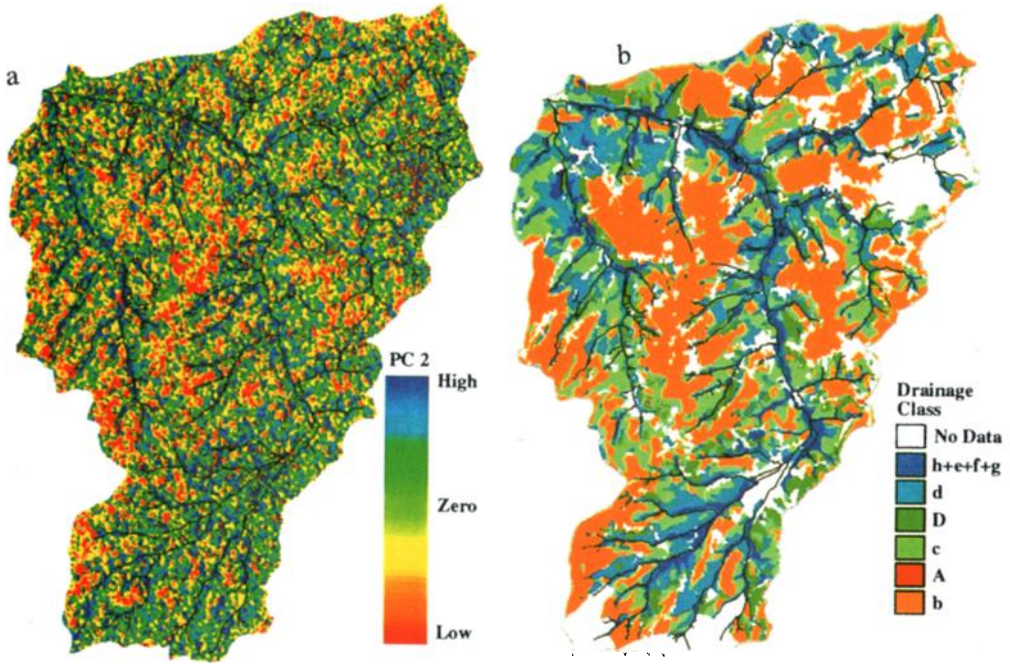

Plate 2. (a) Second principal component image and (b) the drainage map for the catchment. The drainage classification scheme is explained in Table 3.

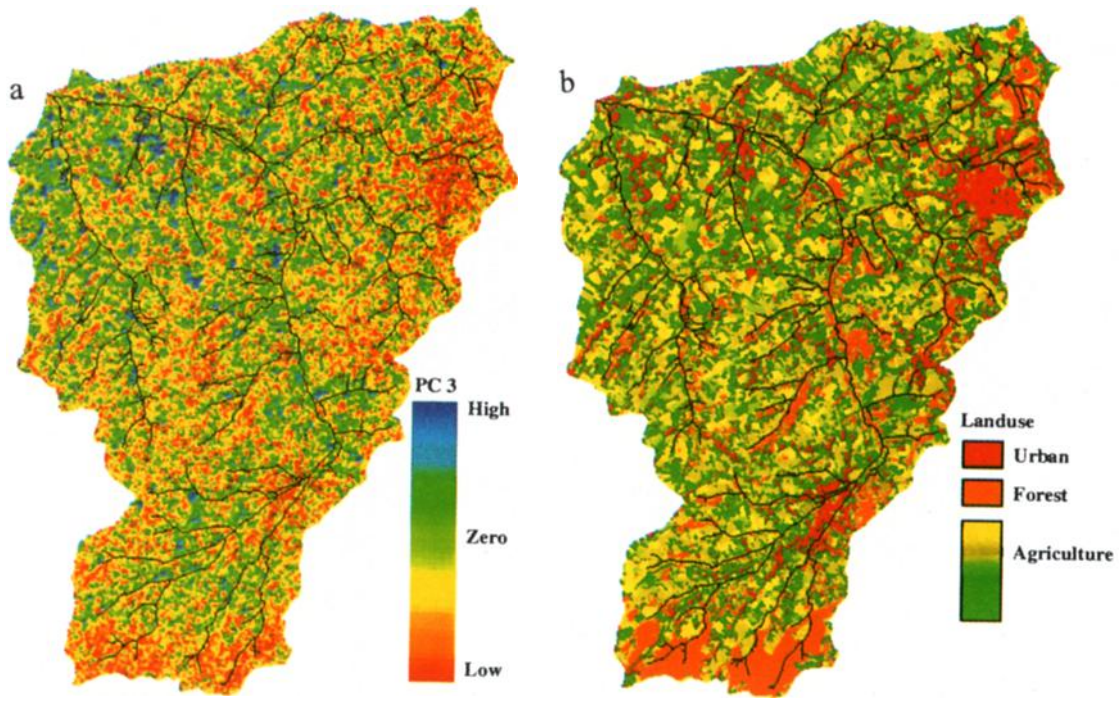

Plate 3. (a) Third principal component image and (b) a classified Landsat image with the forested and urbanized regions in the catchment highlighted.

tion compression. Another example is given by *Henebry* [1997], who used PCA on a temporal series of 12 images for the production of a high spatial resolution/low spatial noise image that served as a template for georeferencing. One of the principal components obtained could then be used for land cover segmentation.

Suppose a PCA is to be performed on M images, each containing P rows and Q columns, or $N = P \times Q$ pixels. We define $\chi_i = [\chi_i(1), \chi_i(2), \cdots, \chi_i(M)]^T$ and $\chi_i(k) = \chi_{pq}(k) =$ pixel(p, q) of image k, with $i = (p - 1)(Q) + q$ and $p{:}1 \rightarrow P$, $q{:}1 \rightarrow Q$, and $k{:}1 \rightarrow M$.

In order to calculate the principal components (PCs), which are the projection coefficients on the principal axes with an orthonormal basis, $E = (E(1), E(2), \ldots, E(M))$, with $E(j)$ being the unit vectors of the new coordinate system, we have to calculate the cross-covariance matrix, C, for which the element $C_{kk'}$ at row k and column k' is the covariance between image k and image k':

$$C_{kk'} = \frac{1}{N-1} \sum_{i=1}^{N} [\chi_i(k) - \overline{\chi(k)}][\chi_i(k') - \overline{\chi(k')}] \quad (3)$$

where $\overline{\chi(k)} = 1/N \sum_{i=1}^{N} \chi_i(k)$.

To determine the principal components transformation it is necessary to find the eigenvalues and eigenvectors of the matrix C. The eigenvalues are given by the solution to the characteristic equation $|C - \lambda \mathrm{I}| = 0$ where I is the identity matrix. The orthonormal basis E can be found by solving

$$\Lambda = (E)(C)(E^T)$$

where

$$\Lambda = \begin{pmatrix} \lambda_1 & 0 & \cdots & 0 \\ 0 & \lambda_2 & \cdots & 0 \\ \vdots & \vdots & \ddots & \vdots \\ 0 & 0 & \cdots & \lambda_M \end{pmatrix}$$

Since the eigenvalues λ_k are the diagonal elements of the covariance matrix in the new coordinate system, they express the variance of the kth principal component [*Vautard et al.*, 1992]. The principal components, $\gamma(k)$, can be calculated as

$$\gamma_i = (E)(\chi_i)$$

for $k = 1, \cdots, M$ and $i = 1, \cdots, N$.

Table 2 summarizes these calculations for our sequence of eight SAR images, while Plates 1–3 show the images constructed for the first three PCs. The results are discussed in detail in section 4.2.

4.2. Results

Applying PCA to the eight images leads to the separation of the information contained in the images into several components that can be attributed to different factors influencing the backscatter. The first principal component accounts for 76.6% of the total variance, the second component accounts for 6.6%, the third accounts for 5.9%, and each of the remaining PCs accounts for <4% (Table 2).

Plate 1a compares the first component with a local incidence angle image computed from the digital elevation model of the catchment. The similarity between these two images suggests that topographic effects are responsible for the largest contribution to the total variance in the sequence of SAR images and dominate the backscattering signal. A sequence of images

Table 2. Coefficients of the Eigenvectors for Each Principal Component and the Total Data Variance Accounted for by Each PC

PC	Matrix of Eigenvectors								Var., %
	Oct. 31, 1995	Nov. 1, 1995	Dec. 5, 1995	Dec. 6, 1995	Feb. 13, 1996	Feb. 14, 1996	March 19, 1996	March 20, 1996	
1	−0.32	−0.32	−0.31	−0.27	−0.44	−0.37	−0.39	−0.37	76.59
2	−0.11	−0.21	0.09	0.45	−0.65	0.54	−0.01	0.12	6.55
3	−0.19	−0.18	−0.31	−0.04	0.50	0.64	−0.30	−0.29	5.94
4	0.67	0.38	−0.02	0.17	−0.15	0.03	−0.46	−0.38	4.00
5	0.40	−0.03	−0.60	−0.47	−0.23	0.23	0.27	0.28	2.59
6	0.26	−0.49	−0.40	0.59	0.23	−0.32	−0.02	0.18	2.01
7	0.41	−0.66	0.52	−0.33	0.05	0.08	−0.05	−0.06	1.47
8	0.06	−0.07	−0.07	0.13	−0.04	0.00	0.68	−0.71	0.84

taken with the same radar configuration and footprint (frame and track) will show a very high correlation: Slopes facing the satellite will consistently return more energy than the slopes turned away from the sensor. The principal component analysis has brought out these highly correlated features in the first PC.

The Plate 2a represents the second principal component. This image displays a strong spatial organization, with the highest values grouped along the drainage network of the catchment. To test the hypotheses that the information contained in this image is related to the drainage conditions of the catchment, a drainage map for the Zwalm was generated and is shown in Plate 2b. The drainage map was derived from the digital soil map of the catchment and classifies the different soils into well-drained and poorly drained classes according to borehole field observations made in the 1960s and 1970s. From the borehole samples, taken approximately every hectare, estimates of the depth to gley and mottle were obtained, from which a drainability index was derived (Table 3). Gley can be described as a blue-grey waterlogged soil layer in which iron is reduced to the ferrous form. This layer can turn into a soil containing brownish mottles due to oxidation of iron during intermittent dry periods. The occurrence of these features therefore indicates the change in water table height between winter (mottle) and summer (gley). As can be seen from Plate 2, the poorly drained soils tend to occur in the valley regions of the catchment and correspond well with the areas with high second PC values. This suggests a radar response, brought out in the second principal component, to the soil moisture patterns that result from the drainage characteristics of the basin. These patterns are not attributable to any single event but reflect the overall response of the soil to the rainfall and interstorm periods spanned by the images, as illustrated by Figure 1.

Table 3. Definition of Natural Drainage Classes According to the Belgian Nomenclature

Drainability Index	Average Winter Water Table Depth (Depth to Mottle), cm	Average Summer Water Table Depth (Depth to Gley), cm
b	>125	...
c	80–125	...
d	50–80	...
h	30–50	...
e	30–50	>80
f	0–30	40–80
g	...	<40
A	>50	...
D	50–125	...

Fields with class A consist of patches of classes b, c, and d and cannot be uniquely defined as one of its constituent classes. Fields with class D contain patches of classes c and d.

The third principal component (Plate 3a) shows the influence of land cover and land use, as evidenced by its strong correlation with the Landsat-derived map (Plate 3b) that highlights the forested areas in the south of the catchment and the few towns in the basin. The land use map is the result of a supervised classification performed on a Landsat TM image of October 12, 1994. The classification resulted in 10 classes, such as woods, urbanized areas, and agricultural fields, which are grouped together as shown in Plate 3. In SAR images, urban areas typically appear as bright objects, and, in a sequence of images, such areas, with their relatively static features, will produce a consistent backscattering signal. If there are few changes in major vegetation features over the same sequence of images, each canopy type will also produce a typical but temporally consistent radar response.

The fourth and subsequent principal components account for a smaller fraction of the total variance in the sequence of SAR images, and they do not seem to reveal significant geophysical features. These PCs are characterized mostly by noise (including speckle).

In order to provide a more objective comparison between the two images in Plate 2, we have calculated the user's and producer's accuracy [*Lillesand and Kiefer*, 1994]. The user's accuracy represents the probability that a pixel classified into a given category actually belongs to that category on the ground. This value can be obtained by dividing the number of correctly classified pixels by the total number of pixels that were classified for that category. The producer's accuracy is the probability that a pixel is classified correctly given a specific category on the ground. This value can be calculated by dividing the number of correctly classified pixels in a category by the total number of pixels for that category. If we assume that the drainage class b corresponds to a PC2 value smaller or equal to 0 and the other classes (except for class A, since it is not clear whether this class consists of dry or wet fields; moreover, the areal coverage of this class is limited in the catchment (see Plate 2) correspond to the positive PC2 values, we find a producer's accuracy for the lumped drainage classes c, D, d, e, f, g, and h of 66.0% and a user's accuracy of 70.5% (see Table 4). This shows that a good representation of the wetter areas is given by the positive PC2 values. Similarly, the producer's and user's accuracy for the class b is 53.0% and 47.8%, respectively. These values are quite low and indicate a less successful representation of the dry areas by the negative PC2 values.

Table 4. Producer's and User's Accuracies for the Principal Component Images in Plates 1–3

	Producer's Accuracy, %	User's Accuracy, %
Figure 4		
PC1 > −850 corresponds to local incidence angle >23°	64.7	55.1
PC1 ≤ −850 corresponds to local incidence angle <23°	64.4	73.0
Figure 5		
PC2 > 0 corresponds to drainage classes c, D, d, e, f, g, and h	66.0	70.5
PC2 ≤ 0 corresponds to drainage classes A and b	53.0	47.8
Figure 6		
PC3 < −20 corresponds to urban and wooded areas	32.0	32.6
PC3 ≥ −20 corresponds to agricultural areas	81.9	81.5

A similar analysis was also performed for Plates 1 and 3, with the results reported in Table 4. The thresholds on the PC image were chosen such that the number of pixels for the corresponding classes in the two images was approximately equal. It is expected that better results for these accuracies could be obtained if the PC images were subjected to classification algorithms which make use of neighborhood functions in order to avoid the influence of small anomalies within the different class polygons. Further research is required to establish more rigorous statistical methodologies for the comparison of two images when one image consists of classified data and the other of linear data, taking into account the spatial correlations within each image.

5. Discussion and Conclusions

From field experiments in small watersheds, it has been shown that parts of the watershed where infiltration capacity is relatively low are the most probable contributing areas during a storm [*Van De Griend and Engman*, 1985]. Low infiltration capacity is related to soil moisture and the following factors: Soil properties are such that they do not allow rapid water movement; groundwater seepage zones maintain near-saturated conditions, and thus very little storage is available for rainfall; soilwater convergence on concave topographical units sustains relatively wet zones; and high antecedent moisture reduces the infiltration capacity of certain soils within the watershed. These factors support the hypothesis that potential partial contributing areas correspond to zones with high soil moisture and low variability in soil moisture and can be related to the discharge zones shown in Figure 1. This strong connection between soil moisture and both partial areas and discharge zones makes it reasonable to assume that these areas can be mapped via observations of soil moisture variability.

As backscattering of microwaves depends in part on the moisture content of the reflecting surface, radar images contain potentially useful data for the hydrologist. However, single images do not reveal much information, as is apparent in Figure 2, owing to the influence of other factors such as surface roughness, vegetation, and speckle. It is the presence of conflicting effects on radar backscatter that informs the use of techniques such as principal component analysis, which is able to transform images to render discernable features that cannot be seen in the original data.

As was described previously, the second principal component shown in Plate 2 appears to reflect the soil moisture response from rainfall and drainage/redistribution episodes and corresponds well with the seasonal drainage conditions of the soil. These links can be strengthened by examining the radar signal's behavior for the negative and positive values of the second principal component. Figure 4 plots, for each SAR image, the average backscatter value of these two classes in the second PC. The negative class generally corresponds to the well-drained soils, which are found upslope, while the positive class mainly coincides with the poorly drained areas (Plate 2). With reference to Figure 1, discharge areas exhibit a lower temporal variability in soil moisture content than the upslope areas, and this is reflected in the lower variability of the radar backscattering for the positive PC2 areas seen in Figure 4. During a drydown period, upslope areas show a larger decline in soil moisture content than near-stream areas, which corresponds to a larger decline in the backscattered signal of the negative PC2 areas for the first four data takes. The large rain event of February 13 is reflected in the large increase in signal for both positive and negative PC2 areas. Over the course of the following 24 hours, soil moisture was redistributed over the basin, leading to a decrease of soil wetness in the recharge zones but little change in the already saturated near-stream zones, as evidenced in Figure 4. Shrinkage of the variable

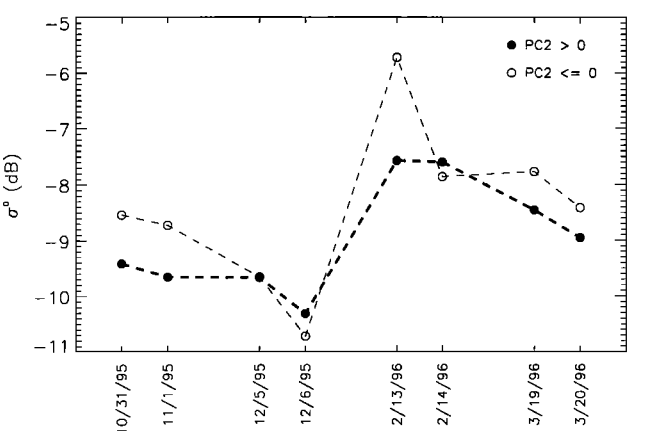

Figure 4. Average radar backscatter values for the negative and positive PC2 values. The time axes is plotted with equal intervals between the tandem pairs of ERS 1/2 images; refer to Figure 3 for the undistorted distribution of the images (and rainfall) over time.

source areas over the following weeks accounts for the decrease of the backscattered signal of the positive PC2 class.

To summarize, this paper examined the ability of active microwave remote sensing to detect or map changes in surface soil moisture at basin scales. The application of PCA to the Zwalm images suggests that the current generation of operational SAR instruments can effectively provide soil moisture information, when used within a multitemporal framework together with analysis techniques that are capable of separating dominant effects from less predominant ones arising from local features or temporal changes. The results presented here are preliminary and need further testing. For instance, to minimize possible effects of changes in local incidence angle, surface roughness, and vegetation, the ERS images were selected for a winter period and share the same frame and track. It will be important to analyze other basins and nonwinter sets of images, both to test the robustness of PCA and to investigate the possibility of identifying not only soil moisture features but also vegetation and/or surface roughness effects in separate higher-order principal components.

Acknowledgments. We acknowledge the financial support of the European Commission through grant EV5V-CT94-0446, the Sardinia Regional Authorities, and the Research Fund of the University of Gent. We thank J. Deckmyn and M. Marrocu for helpful discussions during the early stages of this research. The eight SAR images analyzed in this paper were supplied by the European Space Agency (ESA).

References

Altese, E., O. Bolognani, M. Mancini, and P. A. Troch, Retrieving soil moisture over bare soil from ERS-1 synthetic aperture radar data: Sensitivity analysis based on a theoretical surface scattering model and field data, *Water Resour. Res.*, *32*(3), 653–661, 1996.

Attema, E., The active microwave instrument on-board the ERS-1 satellite, *Proc. IEEE*, *79*, 791–799, 1991.

Blyth, K., The use of microwave remote sensing to improve spatial parameterization of hydrological models, *J. Hydrol.*, *152*, 103–129, 1993.

Capehart, W. J., and T. N. Carlson, Decoupling of surface and near-surface soil water content: A remote sensing pespective, *Water Resour. Res.*, *33*(6), 1383–1395, 1997.

Choudhury, B. J., Multispectral satellite data in the context of land surface heat balance, *Rev. Geophys.*, *29*(2), 217–236, 1991.

Cognard, A.-L., C. Loumagne, M. Normand, P. Olivier, C. Ottlé, D. Vidal-Madjar, S. Louahala, and A. Vidal, Evaluation of the ERS 1/synthetic aperture radar capacity to estimate surface soil moisture: Two-year results over the Naizin watershed, *Water Resour. Res.*, *31*(4), 975–982, 1995.

Construction Engineering Research Laboratories (CERL), *Grass 4.1 Installation Guide*, Champaign, IL, 1993. (Available at http://www.baylor.edu/~grass/4.1release.info.html.)

De Troch, F., *Studie van de oppervlaktewaterhydrologie van een Oost-Vlaams stroombekken: de Zwalmbeek te Nederzwalm* (in Dutch), Ph.D. dissertation, Univ. of Gent, Gent, Belgium, 1977.

De Troch, F., P. Troch, Z. Su, and D. S. Lin, Application of remote sensing for hydrological modelling, in *Distributed Hydrological Modelling*, edited by M. Abbott and J. C. Refsgaard, pp. 165–191, Kluwer Acad., Norwell, Mass., 1996.

De Troch, F., P. A. Troch, and Z. Su (Eds.), Spatial and temporal soil moisture mapping from ERS-1 and JERS-1 SAR data and macroscale hydrologic modelling, *EV5V-CT94-0446 proj. rep.*, EC-Environment and Climate Research Programme, Laboratory of Hydrology and Water Management, Gent, Belgium, 1997.

Engman, E. T., Recent advances in remote sensing in hydrology, *U.S. Natl. Rep. Int. Union Geod. Geophys. 1991–1994, Rev. Geophys.*, *33*, 967–975, 1995.

European Space Agency, (ESA), ESA ERS-1 Product Specification, Tech. Rep., Eur. Space Agency, Frascati, Ital., 1992.

Georgakakos, K. P., and O. W. Baumer, Measurement and utilization of on-site soil moisture data, *J. Hydrol.*, *184*, 131–152, 1996.

Gineste, P., C. Puech, and P. Mérot, Radar remote sensing of the source areas from the Coët-Dan catchment, *Hydrol. Proc.*, *12*, 267–284, 1998.

Goodman, J., Some fundamental properties of speckle, *J. Opt. Soc. Am.*, *66*(11), 1145–1150, 1976.

Henebry, G. M., Advantages of principal components analysis for land cover segmentation from SAR image series, paper presented at 3rd ERS Symposium on Space at the Service of Our Environment, European Space Agency Publications Division, Noordwijk, Netherlands, 1997.

Hollenbeck, K. J., T. J. Schmugge, G. M. Hornberger, and J. R. Wang, Identifying soil hydraulic heterogeneity by detection of relative change in passive microwave remote sensing observations, *Water Resour. Res.*, *32*(1), 139–148, 1996.

Howarth, J., and G. Wickware, Procedure for change detection using landsat digital data, *Int. J. Remote Sens.*, *2*(3), 277–291, 1981.

Jackson, T. J., Soil moisture estimation using special satellite microwave/imager satellite data over a grassland region, *Water Resour. Res.*, *33*(6), 1475–1484, 1997.

Jenson, J. R., and D. Toll, Detecting residential land use development at the urban fringe, *Photogramm. Eng. and Remote Sens.*, *48*, 629–643, 1982.

Laur, H., P. Bally, P. Meadows, J. Sanchez, B. Schaettler, and E. Lopinto, ERS SAR calibration: Derivation of backscattering coefficient σ^0 in ESA ERS SAR PRI products, Tech. Rep., Eur. Space Agency, Frascati, Ital., 1997.

Lee, J., and K. Hoppel, Principal components transformation of multifrequency polarimetric SAR imagery, *IEEE Trans. Geosc. Remote Sens.*, *30*(4), 686–696, 1992.

Lee, J., I. Jurkevich, P. Dewaele, P. Wambacq, and A. Oosterlinck, Speckle filtering of synthetic aperture radar images: A review, *Remote Sens. Rev.*, *8*, 313–340, 1994.

Lillesand, T. M., and R. W. Kiefer, *Remote Sensing and Image Interpretation*, John-Wiley, New York, 1994.

Lopes, A., H. Laur, and E. Nezry, Statistical distribution and texture in multilook and complex SAR images, paper presented at International Geoscience and Remote Sensing Symposium (IGARSS), Washington, D. C., 1990.

Mattikalli, N. M., E. T. Engman, L. R. Ahuja, and T. J. Jackson, A GIS for spatial and temporal monitoring of microwave remotely sensed soil moisture and estimation of soil properties, in *Application of Geographic Information Systems in Hydrology and Water Resources Management*, edited by K. Kovar and H. P. Nachtnebel, *IAHS Publ.*, *211*, 621–628, 1996.

Nezry, E., A. Lopes, and R. Touzi, Detection of structural and textural features for SAR images filtering, paper presented at International Geoscience and Remote Sensing Symposium (IGARSS), Espoo, Finland, 1991.

Porcello, L., N. Massey, R. Innes, and J. Marks, Speckle reduction in synthetic-aperture radars, *J. Opt. Soc. Am.*, *66*(11), 1305–1311, 1976.

Richards, J. A., *Remote Sensing Digital Image Analysis*, Springer-Verlag, New York, 1986.

Rignot, E., and J. van Zyl, Change detection techniques for ERS-1 SAR data, *IEEE Trans. Geosc. Remote Sens.*, *31*(4), 896–906, 1993.

Salvucci, G. D., Soil and moisture independent estimation of stage-two evaporation from potential evaporation and albedo or surface temperature, *Water Resour. Res.*, *33*(1), 111–122, 1997.

Salvucci, G. D., and E. Amano, Surface and satellite estimates of the transition between soil and atmosphere limits on evaporation, *Eos Trans. AGU*, *78*(17), *Spring Meet. Suppl.*, S142, 1997.

Salvucci, G. D., and D. Entekhabi, Hillslope and climatic controls on hydrologic fluxes, *Water Resour. Res.*, *31*(7), 1725–1739, 1995.

Schwan, H., S. Wunderle, and Y.-L. Desnos, Evaluation of speckle-filtered ERS-1 SAR images in Patagonia and Antartica, *Earth Obs. Q.*, *49*, 17–20, 1995.

Shi, Z., and K. B. Fung, A comparison of digital speckle filters, paper presented at International Geoscience and Remote Sensing Symposium (IGARSS), Pasadena, Calif., 1994.

Singh, A., Digital change detection techniques using remotely-sensed data, *Int. J. Remote Sens.*, *10*(6), 989–1003, 1989.

Su, Z., P. A. Troch, and F. P. De Troch, Remote sensing of soil moisture using EMAC/ESAR data, *Int. J. Remote Sensing*, *18*(10), 2105–2124, 1997.

Ulaby, F., T. Haddock, and R. Austin, Fluctuation statistics of milli-

meter-wave scattering from distributed targets, *IEEE Trans. Geosc. Remote Sens.*, *26*(3), 268–281, 1988.

Ulaby, F. T., R. K. Moore, and A. K. Fung, *Microwave Remote Sensing, Active and Passive*, vol. 2, Artech House, Norwood, Mass., 1982.

Ulaby, F. T., P. C. Dubois, and J. van Zyl, Radar mapping of surface soil moisture, *J. Hydrol.*, *184*, 57–84, 1996.

Van De Griend, A. A., and E. Engman, Partial area hydrology and remote sensing, *J. Hydrol.*, *81*, 211–251, 1985.

Vautard, R., P. Yiou, and M. Ghil, Singular-spectrum analysis: A toolkit for short, noisy chaotic signals, *Physica D*, *58*, 95–126, 1992.

Verhoest, N., ERS SAR calibration of preliminary georeferenced images, Tech. Rep., Laboratory of Hydrology and Water Management 1997. (Available at http://taoren.rug.ac.be/~niko/ERScalib.html.)

Wagner, W., M. Borgeaud, and J. Noll, Soil moisture mapping with the ERS scatterometer, *Earth Obs. Q.*, *54*, 4–7, 1996.

F. P. De Troch, P. A. Troch, and N. E. C. Verhoest, Laboratory of Hydrology and Water Management, University of Gent, Coupure Links 653, 9000 Gent, Belgium. (e-mail: Niko.Verhoest@rug.ac.be)

C. Paniconi, Centro di Ricerca, Sviluppo e Studi Superiori in Sardegna (CRS4), Via Nazario Sauro 10, 09123 Cagliari, Italy.

(Received February 6, 1998; revised June 11, 1998;
accepted June 16, 1998.)